

Electrically Tunable and Dramatically Enhanced Valley-Polarized Emission of Monolayer WS₂ at Room Temperature with Plasmonic Archimedes Spiral Nanostructures

Wei-Hsiang Lin,* Pin Chieh Wu, Hamidreza Akbari, George R. Rossman, Nai-Chang Yeh,* and Harry A. Atwater*

Monolayer transition metal dichalcogenides (TMDs) have intrinsic valley degrees of freedom, making them appealing for exploiting valleytronic applications in information storage and processing. WS₂ monolayer possesses two inequivalent valleys in the Brillouin zone, each valley coupling selectively with a circular polarization of light. The degree of valley polarization (DVP) under the excitation of circularly polarized light (CPL) is a parameter that determines the purity of valley polarized photoluminescence (PL) of monolayer WS₂. Here efficient tailoring of valley-polarized PL from monolayer WS₂ at room temperature (RT) through surface plasmon–exciton interactions with plasmonic Archimedes spiral (PAS) nanostructures is reported. The DVP of WS₂ at RT can be enhanced from <5% to 40% and 50% by using 2 turns (2T) and 4 turns (4T) of PAS, respectively. Further enhancement and control of excitonic valley polarization is demonstrated by electrostatically doping monolayer WS₂. For CPL on WS₂–2TPAS heterostructures, the 40% valley polarization is enhanced to 70% by modulating the carrier doping via a backgate, which may be attributed to the screening of momentum-dependent long-range electron–hole exchange interactions. The manifestation of electrically tunable valley-polarized emission from WS₂–PAS heterostructures presents a new strategy toward harnessing valley excitons for application in ultrathin valleytronic devices.

1. Introduction

Monolayer 2H-phase transition metal dichalcogenides (TMDs) MX₂ are direct-bandgap semiconductors that consist of an atomic layer of transition metal atoms (M) sandwiched between a top and a bottom layer of halogen atoms (X) that are arranged in their respective hexagonal lattice structure.^[1,2] The band structures of monolayer TMDs^[3–7] consist of two inequivalent K (–K) valleys in the hexagonal Brillouin zone. The strong spin-orbit coupling and broken inversion symmetry in monolayer 2H-TMDs result in a large energy splitting between the top spin-up (spin-down) and bottom spin-down (spin-up) valence bands in the K (–K) valley.^[8–13] This spin-valley coupling gives rise to valley-dependent optical selection rules:^[14–16] circularly polarized light with positive helicity (σ^+) couples to the K valley and that of the negative helicity (σ^-) couples to the –K valley. It is therefore possible to selectively populate and manipulate the different valleys (K or –K) by means of circularly polarized light (CPL).^[11,15]

The spin and valley degrees of freedom (DOF) in these monolayer TMDs materials provide an important platform for exploring new condensed matter physics and for applications in spintronic and valleytronic devices. Noting that the control of circularly polarized emission of light is also a key step toward developing functional optical devices for applications in display technologies^[17,18] and quantum information processing/communication,^[19–21] manipulation of the valley DOF is one of the promising approaches to achieving practical information processing devices that are more energy efficient than existing charge-based technologies.

Although accessing different valley DOF through CPL has been demonstrated in several TMDs, including molybdenum disulfide (MoS₂),^[8–10] molybdenum diselenide (MoSe₂),^[22] tungsten disulfide (WS₂),^[13,23] and tungsten diselenide (WSe₂),^[24–27] it has been challenging to manipulate the valley polarization and the resulting photoluminescence (PL) of monolayer 2H-TMDs at room temperature (RT) because of the weak light-matter interaction and substantial defects^[13] in these atomically

W.-H. Lin, H. Akbari, H. A. Atwater
Department of Applied Physics
California Institute of Technology
Pasadena, CA 91125, USA
E-mail: whlin@alumni.caltech.edu; haa@caltech.edu

P. C. Wu
Department of Photonics
National Cheng Kung University
Tainan 70101, Taiwan

G. R. Rossman
Department of Geological and Planetary Sciences
California Institute of Technology
Pasadena, CA 91125, USA

N.-C. Yeh
Department of Physics
California Institute of Technology
Pasadena, CA 91125, USA
E-mail: ncyeh@caltech.edu

 The ORCID identification number(s) for the author(s) of this article can be found under <https://doi.org/10.1002/adma.202104863>.

DOI: 10.1002/adma.202104863

thin layers. Various approaches, such as applying an in-plan electric field,^[24,28] an out-of-plan magnetic field,^[29–33] or a localized magnetic field,^[34] have been proposed in an attempt to enhance the circular dichroism (CD) of PL in these TMDs.

An alternative approach to enhancing the CD of PL in TMDs is by means of chiral plasmonic metasurfaces.^[34–43] This approach is based on the strong optical chirality in metallic chiral metasurfaces and the enhancement of light-matter interaction through localized surface plasmon resonance (LSPR) modes. Specifically, the confined LSPR modes can strongly interact with the carriers within the monolayer TMD material to form a compact, functional nanophotonic devices. Furthermore, the geometry-dependent LSPR modes of chiral plasmonic metasurface provide wavelength tunability for the wide emission range of different TMDs. Thus, implementing chiral plasmonic metasurfaces^[44–54] on 2H-TMDs is likely an efficient approach to manipulating the CD of PL in these monolayer materials.

In this study, a metal–dielectric–metal (MDM) structure that consists of monolayer WS₂ and plasmonic Archimedes spiral (WS₂–PAS) nanostructures is designed to investigate the monolayer WS₂ exciton-plasmon interaction and to manipulate the valley-polarized PL in WS₂–PAS heterostructures by spectroscopic measurements and numerical simulations. The device configuration included a monolayer WS₂ single crystal grown by chemical vapor deposition (CVD) and transferred to a substrate of 60 nm-thick SiO₂ on top of a 150 nm-thick gold reflection layer. A 60 nm-thick gold film was subsequently deposited on the WS₂/SiO₂/Au structure, and then either righthanded (RH) or lefthanded (LH) spiral gold rings were patterned on the gold film by E-beam lithography. To demonstrate the crystallinity of our monolayer WS₂ samples, we performed Raman spectroscopic studies of the A_{1g} and E_{2g}¹ modes using a 514.3 nm laser (2.41 eV) as the excitation source. Additionally, X-ray photoelectron spectroscopy (XPS) was conducted to examine the chemical composition and valence states of monolayer WS₂, as detailed previously.^[13] Representative Raman and XPS characterization results of a monolayer WS₂ are given in Figures S1 and S2, Supporting Information, respectively.

The magnitude of the degree of valley polarization (DVP) in as-grown monolayer WS₂ was <5% at RT, whereas those of the DVP in monolayer WS₂–2TRHPAS (with 2 turns of RHPAS) and WS₂–4TRHPAS (with 4 turns of RHPAS) under the excitation of right-handed circularly polarized (RCP) light were found to be 40% and 50%, respectively. Here the DVP value (P_{DVP}) is defined by the following expression:

$$P_{\text{DVP}} = \frac{I(\sigma^+) - I(\sigma^-)}{I(\sigma^+) + I(\sigma^-)} \quad (1)$$

where $I(\sigma^+)$ and $I(\sigma^-)$ denote the right- and left-handed circular polarization-resolved PL intensity, respectively. In contrast, the corresponding values of the DVP under the excitation of left-handed circularly polarized (LCP) light decreased to ≈5% in both monolayer WS₂–2TRHPAS and WS₂–4TRHPAS heterostructures. Additionally, the DVP values could be further enhanced by applying a back-gated voltage V_{Gate} from 40% for $V_{\text{Gate}} = 0$ up to 70% for $V_{\text{Gate}} = -20$ V. This finding suggests that modulating the carrier doping level can enhance the valley polarization by

screening the long-range electron–hole exchange interactions, thus reducing the momentum-dependent intervalley scattering. The capability of enhancing and tuning the DVP in monolayer 2H-TMDs at RT by plasmonic chiral metasurfaces and electrical gating offers new opportunities toward developing valley-dependent optoelectronic devices for energy-efficient information processing.

Our proposed underlying mechanism for tailoring the valley-polarized PL of monolayer 2H-WS₂ by PAS and gated voltage is schematically shown in **Figure 1a–c**: in WS₂ monolayer, excitons in the K valley couple with the RCP light (σ^+), whereas excitons in the –K valley couple with the LCP light (σ^-). However, after σ^+ light excitation, the exciton population pumped in the K valley could be scattered to the –K valley due to phonon- and defect-induced intervalley scattering. Therefore, the DVP of PL was usually low at RT as show in **Figure 1a**. On the other hand, when WS₂ monolayer interacts with the RHPAS structures in the near-field range, optical absorption is enhanced, which contributes to more σ^+ excitons under the RCP light in the WS₂–RHPAS structure. In the K valley, the σ^+ excitons interact with the RH chiral near-field of the surface plasmon polaritons (SPP) of PAS, leading to giant optical activities that contribute to enhance the PL intensity in the far field, as shown in **Figure 1b**. In contrast, the σ^- exciton emission generated from –K valley is suppressed by the interaction with the RH chiral near-field. The interplay of exciton generation, exciton emission, and intervalley scattering in each valley contributes to far-field measurements of the valley-polarized PL spectra. As schematically shown in **Figure 1a**, the DVP of the PL emission depends on the decay rates of the excitons at K (γ_K) valley, –K valley (γ_{-K}), and the intervalley scattering rate between the two valleys. Therefore, the DVP can be enhanced through increasing the decay rates of the valley-polarized excitons or decreasing the intervalley scattering rate in two valleys by the chiral Purcell effect. Although the presence of RHPAS structures contributes to increasing the decay rate of the σ^+ excitons, the intervalley scattering is still significant so that the DVP enhancement is limited. The latter situation may be mitigated by applying a gate voltage between the WS₂ and the gold mirror, as shown in **Figure 1c**, so that the excess carrier doping helps screen the momentum-dependent long-range electron–hole exchange interaction, thereby reducing the intervalley scattering and leading to significantly enhanced DVP in gated WS₂–RHPAS heterostructures.

2. Results and Discussion

Coupling TMDs with chiral plasmonic metasurfaces can enhance the light–matter interaction through the confined localized surface plasmon and can be a promising approach to enhance the CD of PL in 2H-TMDs. **Figure 2a** is a schematic illustration of the MDM structure that consists of a monolayer WS₂ and plasmonic Archimedes spiral nanostructures (WS₂–PAS) under the excitation of CPL. The WS₂ monolayer was grown by chemical vapor deposition (CVD) method and then transferred onto a substrate consisting of a 60 nm-thick SiO₂ layer on top of a 150 nm-thick gold mirror layer. The Archimedes spiral rings were patterned by E-beam lithography

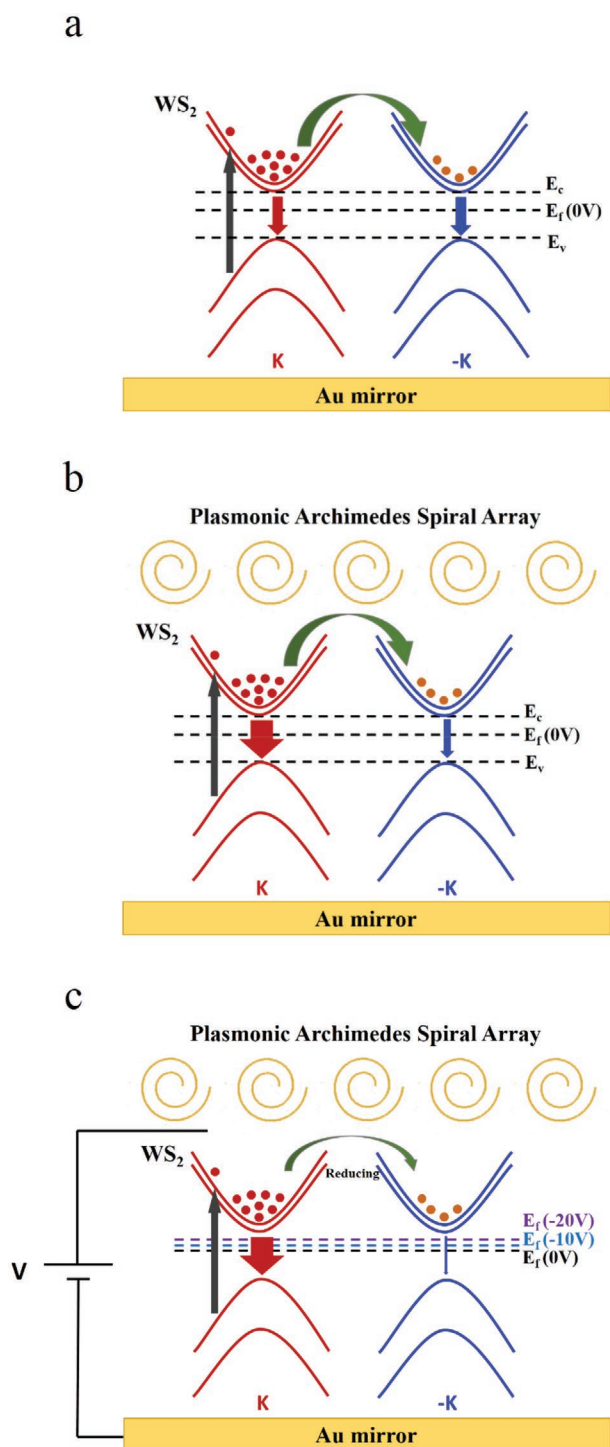


Figure 1. Proposed mechanism for tailoring the valley-polarized PL of gated WS₂-RHPAS heterostructure. a) Schematics of the energy bands of monolayer WS₂ under RCP light with significant intervalley scattering. b) Schematics of the energy bands of monolayer WS₂-RHPAS heterostructure under RCP light, showing significantly increased decay rate of σ^+ excitons. c) Schematics of the energy bands of a gated monolayer WS₂-RHPAS heterostructure, showing both increased decay rate of σ^+ excitons and suppressed intervalley scattering due to carrier doping-induced screening of the long-range electron-hole interaction.

on a 50 nm-thick Au film deposited on the top of the WS₂ monolayer.

Figure 2b shows the PL intensity differences between the as-grown monolayer WS₂ and the MDM structure of a monolayer WS₂ integrated with right-handed plasmonic Archimedes spiral (RHPAS) nanostructures. Under the excitation of right-hand circularly polarized light (RCP, red), the PL intensity of the WS₂-2TPAS heterostructure was enhanced by more than ten times relative to that of the as-grown WS₂ (green). In contrast, the PL intensity was barely enhanced under the excitation of left-handed circularly polarized light (LCP, blue). The strong polarization contrast is a good indicator for exciton-plasmon coupling, and the quantitative strength can be characterized by the intensity enhancement factor (EF). The enhancement factor (EF) is defined as $EF = I_{wi}/I_{wo}$, where I_{wi} (I_{wo}) is the maximum intensity of WS₂ with (without) the Archimedes spiral nanostructures. Figure 2b shows the EF is larger than 10 between the RCP emission of the WS₂-2TPAS and that of the as-grown WS₂, whereas the EF is nearly 1 between the LCP emission of the WS₂-2TPAS and that of the as-grown WS₂. This spectroscopic phenomenon suggests that coupling WS₂ with PAS nanostructures is an efficient way for tailoring the exciton-plasmon interaction through actively controlling the polarization of the incident light. The inset of Figure 2b is a scanning electron microscopy (SEM) image of arrays of WS₂-2TPAS heterostructure, where the scale bar represents 5 μ m.

To understand the enhancement of PL intensity and valley polarization, we note that in the saturation regime, the EF consists of contributions from three processes: an enhanced absorption rate (α), an enhanced light extraction factor (ϵ), and a total rate enhancement factor (γ_{on}/γ_{off}) from the Purcell effect that includes both radiative and nonradiative rates as well as metallic losses. Thus, we have $EF = \alpha\epsilon(\gamma_{on}/\gamma_{off})$, where γ_{on} is the total decay rate of WS₂ coupled to the PAS nanostructures, and γ_{off} is the total decay rate of the as-grown WS₂. The total rate enhancement factor can be directly determined by the time-resolved PL measurements. As shown in Figure S3, Supporting Information, the extracted decay time of the as-grown WS₂ was 1.5 ns ($\tau_{off} = 1/\gamma_{off}$), whereas that for the WS₂-2TPAS was 0.3 ns ($\tau_{on} = 1/\gamma_{on}$). The WS₂-2TPAS heterostructures displayed a significantly faster decay rate and the total rate enhancement was found to be $(\gamma_{on}/\gamma_{off}) \approx 5$ ($\approx 500\%$). Therefore, the underlying Purcell factor (F_p) could be estimated from the relation $F_p = \left(\frac{F_p \gamma_R}{F_p \gamma_R + \gamma_M} \right) \left(\frac{\gamma_{on}}{\gamma_{off}} - 1 \right) \eta_{off}^{-1}$, as detailed in Section S2, Supporting Information. Here γ_R and γ_M are the radiative and metallic-loss decay rates, respectively, and $\eta_{off} \equiv \gamma_R/(\gamma_R + \gamma_{NR})$ represents the quantum efficiency of the as-grown WS₂, where γ_{NR} is the non-radiative decay rate of WS₂. From the measured value $(\gamma_{on}/\gamma_{off}) \approx 5$ and using $\left(\frac{F_p \gamma_R}{F_p \gamma_R + \gamma_M} \right) \approx 1$ in the limit of a large F_p and taking $\eta_{off} = 0.1$,^[24–27] we obtained an underlying Purcell factor $F_p \approx 40$. The coupling factor $\beta \equiv F_p/(1 + F_p)$ thus estimated was around 98%, which implied that nearly all the PL emission was coupled to the MDM nanocavity mode.

The exciton-plasmon interaction in WS₂-PAS nanostructures is dependent on the incident laser power, the PL intensity of the as-grown WS₂, and the specific designs of the

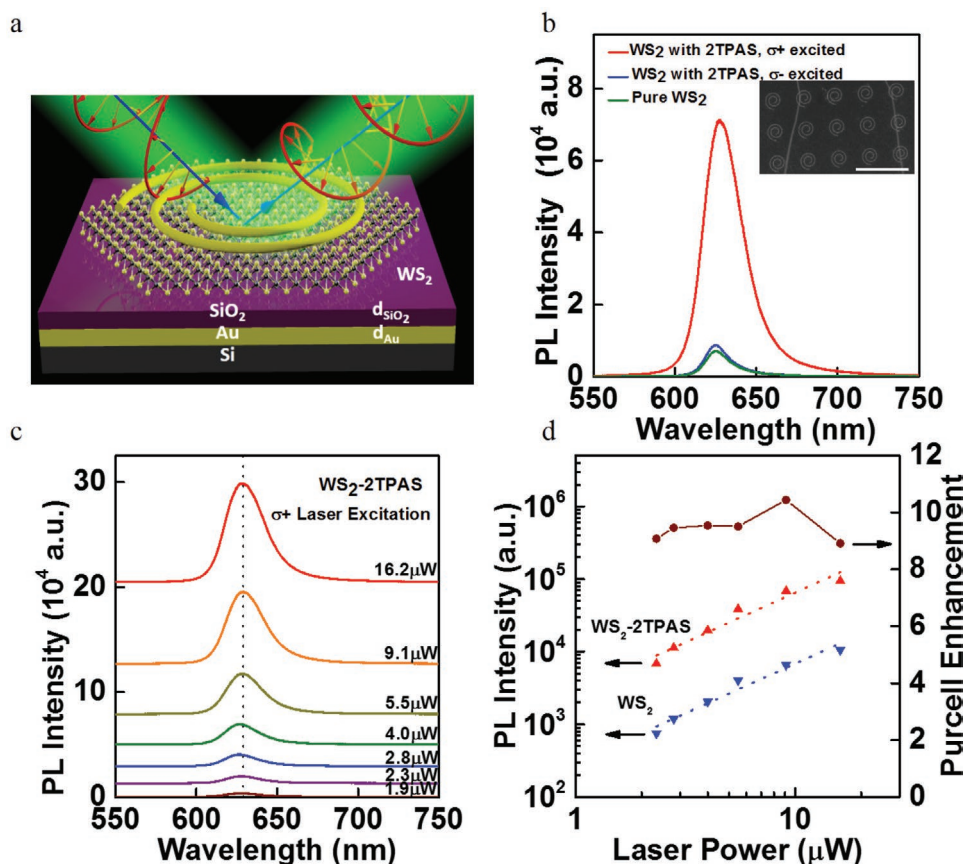


Figure 2. Structure and optical spectral properties of monolayer WS₂ integrated with two turns (2T) of a right-handed plasmonic Archimedes spiral (WS₂-2TRHPAS) heterostructures, where the resonance wavelength of the PAS (R_{plasmon}) is 620 nm. a) Schematics of a WS₂-2TRHPAS heterostructure under CPL excitations, where a CVD-grown monolayer WS₂ is placed on top of an SiO₂ layer sandwiched between Au spiral structures and an Au film. b) PL spectra of monolayer WS₂ with and without the Au spiral structures, under the excitation of different CPL at 514 nm and the laser power at 8.8 μW. The inset shows an SEM image of the WS₂-2TRHPAS array and the scale bar is 5 μm. c) Evolution of the PL spectra of monolayer WS₂-2TRHPAS with laser power. d) Power-dependent PL intensity with (red) and without (blue) Au spiral nanostructures and the corresponding Purcell enhancement (dark red).

Archimedes spiral nanostructures. The laser power dependence of PL, under 514 nm RCP laser excitation in WS₂-2TRHPAS with RH spiral nanostructures, was revealed in Figure 2c. The PL intensity of the WS₂-2TRHPAS was found to increase rapidly with the laser power from 1.9 to 16.2 μW, and the PL peak position also exhibited a slight blue shift with increasing laser power up to 5.5 μW, and then remained invariant from 5.5 to 16.2 μW. Figure 2d presented a log-log plot of the power-dependent PL intensity of WS₂ with (red, triangle) and without (blue, inverted triangle) the plasmonic coupling effect. The relationship between PL intensity (I_{PL}) and laser power (P_{laser}) could be approximately expressed by the relation $I_{\text{PL}} = (P_{\text{laser}})^m$, where m denoted a constant. For both WS₂ with and without spiral structures, the corresponding m values were fitted to be ≈ 1.37 for laser powers ranging from 1.9 to 16.2 μW, and a maximum enhancement factor ϵ reached >10 at 9.1 μW.

Valley polarization in monolayer TMDs could be induced by CPL excitations and detected by PL measurements at RT. Figure 3 shows the comparison of the valley polarized PL spectra between an as-grown monolayer WS₂ and a WS₂-2TRHPAS heterostructure under the excitations of RCP and LCP light. The wavelength of the excitation laser was

514 nm ($E_{\text{pump}} = 2.41$ eV), which was far away the neutral exciton resonant energy ($E_{\text{X}} = 2$ eV). A linear polarizer and a quarter-wave plate (400–800 nm) were placed after the laser to obtain CPL. The polarized PL signal was resolved by a broadband polarizer and a quarter-wave plate placed before the spectrometer.

The representative PL spectra of the as-grown WS₂ single crystal exhibited similar behavior under both the RCP and LCP excitations, as shown in Figure 3a,d. The obtained DVP ($<5\%$) was consistent with previous studies at RT. According to the valley-dependent optical selection rule of TMDs, σ^{\pm} (σ) excitations only coupled to the specific excitonic transitions in the K (-K) valley so that the corresponding light emission should have carried single handedness. However, as schematically shown in Figure 1, when the K valley was selectively excited by σ^+ polarized light, the PL emission contained not only σ^+ signals from polarized excitonic transitions in the K valley but also σ^- signals from the -K-valley, which may be primarily attributed to optical phonon-assisted intervalley scattering of excitons from K to -K-valley, with spin angular momentum exchanged at a finite rate.

As shown in Figure 3b, the PL intensity of the σ^+ emission spectra from the WS₂-RHPAS heterostructure was significantly

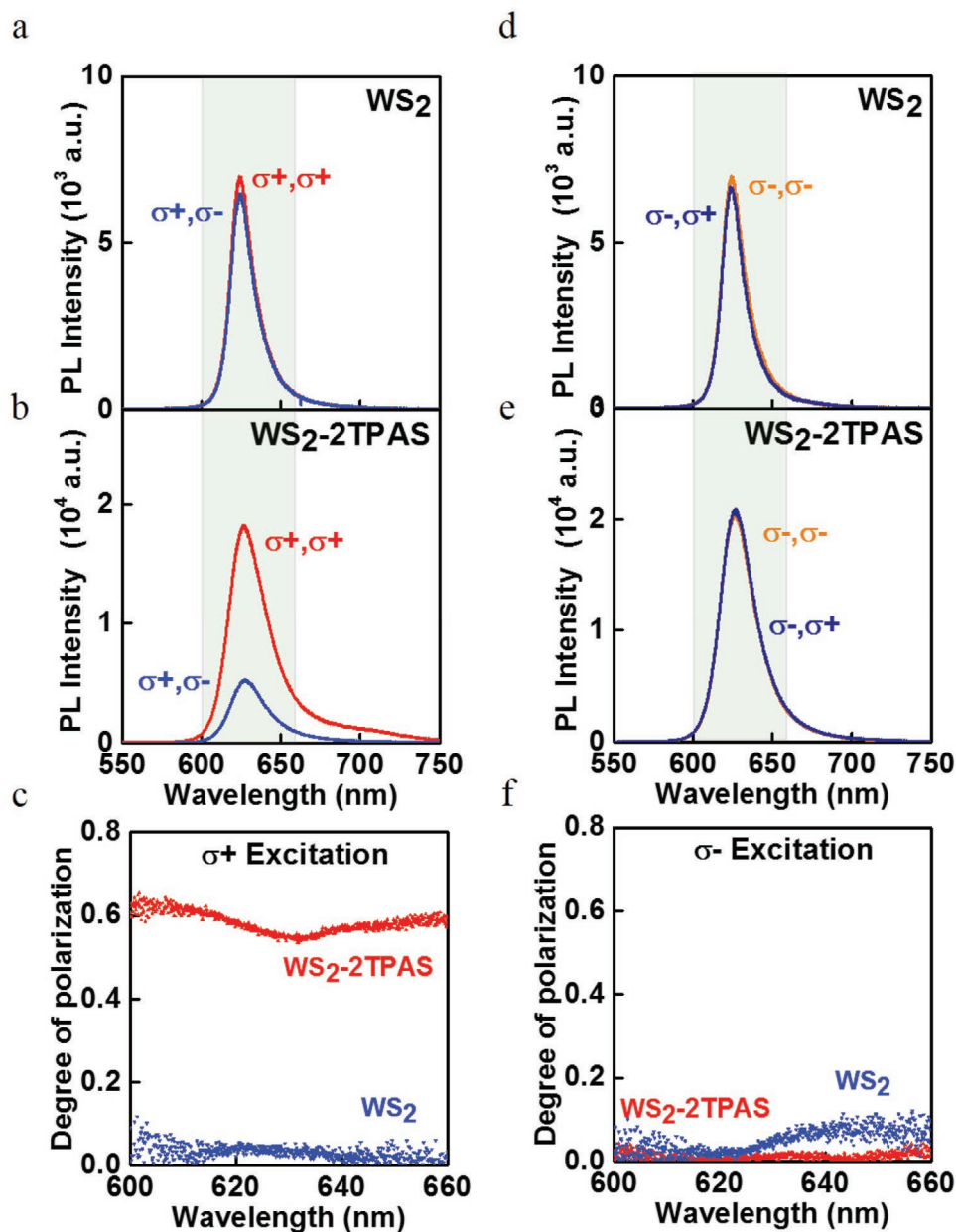


Figure 3. Valley-polarized PL spectra of the as-grown WS₂ and WS₂-2TRHPAS. a,b) Circularly polarized PL spectra of WS₂ and WS₂-2TRHPAS under the excitation of σ^+ light (514 nm) at RT. d,e) Circularly polarized PL spectra of WS₂ and WS₂-2TRHPAS under the excitation of σ^- light (514 nm) at RT. c,f) The degrees of valley polarization (DVP) spectra associated with WS₂ and WS₂-2TRHPAS for σ^+ excitations (c) and for σ^- excitations (f).

enhanced relative to that of the σ^- emission spectra under the σ^+ excitation. In contrast, the PL intensity of the σ^+ and σ^- emission spectra from the WS₂-2TRHPAS heterostructure did not exhibit any enhancement under the σ^- excitation, as shown in Figure 3e. For comparison between the DVP under σ^+ and σ^- excitations, the corresponding DVP spectra are shown in Figures 3c and 3f for the as-grown WS₂ and the WS₂-2TRHPAS heterostructure, respectively. We find that the value of DVP from the WS₂-2TRHPAS heterostructure increased to $\approx 55\%$ under the σ^+ excitation and decreased to $\approx 1\%$ under the σ^- excitation. These notable DVP values of the WS₂-2TRHPAS

may be attributed to the nontrivial interaction between the excitons in WS₂ and the chiral plasmonic mode in the PAS.

To better understand the exciton-plasmon interactions, we further investigated the effect of different plasmonic structures on the valley-polarized PL spectra. Figure S4a, Supporting Information, shows the SEM image of 2-turn RHPAS, and the structural parameters of the PAS are given in Figure S4b, Supporting Information. The spiral structure has an inner radius $r_0 = 200$ nm, width = 50 nm, and pitch = 310 nm so that the outer radius $r = r_0 + N(R_{\text{Plasmon}}/2)$, where N is the integer number of turns and $R_{\text{Plasmon}} = 620$ nm is the resonance

wavelength of the surface plasmon polariton, which coincides with the neutral A-exciton emission wavelength in the PL spectrum of monolayer WS₂. These structure parameters were chosen by the COMSOL simulation results (Figures S4 and S5, Supporting Information) so that strong field enhancement could be achieved at the ring center under the RCP excitation. Moreover, the pitch of the spiral must match the wavelength of the surface plasmon polariton (SPP). Overall, proper choices of the structural parameters are essential to optimize the exciton-plasmon interaction in the PAS structures.

Figure S4c, Supporting Information, shows the near-field PL intensity in the *x*-*y* plane under RCP excitation. When a 2-turn RHPAS interacted with the RCP light, the surface plasmon polaritons (SPPs) were generated by the RH spiral structures and coherently propagated toward to the ring center to form a constructive focus point. The excitons thus generated (RCP emission) interacted constructively with the SPP field, which resulted in enhanced PL intensity at the center of the RH spiral structure. Figure S4e, Supporting Information, shows the corresponding phase map of the 2-turn RHPAS in the *x*-*y* plane under RCP excitations. The phase at the center of the spiral ring revealed a locally uniform phase distribution as shown by the white dotted circle in Figure S4e, Supporting Information. Thus, the constructive interaction of excitons and SPP fields resulted in significant PL enhancement under the RCP excitation. In contrast, the LCP excitation induced weak E-field distribution without focusing effects, as shown in Figure S4d, Supporting Information. At the center of the spiral ring the phase varied from $-\pi$ to π as shown in Figure S4f, Supporting Information. The SPPs propagated as before with the LCP excitation, but the phase could not compensate to yield constructive, focusing effects at the center of the spiral structure.

Interestingly, the E-field and phase distribution were also dependent on the number of turns of the PAS, and the dependence of the exciton-plasmon interaction on the number of turns is manifested in Figure 4 and Figure S5, Supporting Information. In Figure 4a–d, we show the SEM images of 1-, 2-, 3-, and 4-turn PAS arrays on a monolayer WS₂ single crystal. The corresponding PL intensity maps under RCP excitation are shown in Figure 4e–h, where it is evident that the PL intensity became dramatically enhanced when the WS₂ monolayer coupled with the 2-turn and 4-turn RH spiral rings. In contrast, the intensity enhancement was insignificant in the case of 1-turn and 3-turn RH spiral rings. The corresponding E-field distributions are shown in Figure S5a–d, Supporting Information, where we found that the focusing effects only happened for the RHPAS structures with an even number of turns. This finding may be explained in terms of the phase compensation effects induced by the outer and inner spiral coupling at subwavelengths. The phase distribution of the PAS heterostructure demonstrated a strong dependence on the number of turns in the spiral structure, as shown in Figure S5e–h, Supporting Information. For PAS with an even number of turns, the phase at the center of the spiral ring revealed a locally uniform phase distribution, as manifested by the white dotted circle Figure S5f and S5h, Supporting Information. In contrast, the phase changed from $-\pi$ to π for PAS with an odd number of turns.

In addition to the PL intensity, spatially resolved DVP maps further revealed that the DVP was also dependent on

the number of turns in the PAS structure and the CP of the light excitations, as shown in Figure 4i–l and Figures S6–S9, Supporting Information, for 1-, 2-, 3-, and 4-turn RHPAS arrays on a monolayer WS₂. For a RHPAS with an odd number of turns, the DVP values under RCP excitations were lower than 10%. In contrast, for a RHPAS with an even number of turns, the DVP values under RCP excitations were much enhanced, ranging from 35% to 55% for 2T-RHPAS and from 40% to 55% for 4T-RHPAS. On the other hand, the DVP values for 2- and 4-turn RHPAS arrays under LCP excitations were uniformly and strongly suppressed (Figures S7 and S9, Supporting Information), whereas those for 1- and 3-turn RHPAS arrays under LCP excitations exhibited significant spatial inhomogeneity (Figures S6 and S8, Supporting Information). Such a strong dependence of the valley polarization associated with the far-field PL mapping of the WS₂-PAS heterostructure may be attributed to the consequences of the near-field interaction between the valley excitons in WS₂ and the surface plasmon modes in the PAS.

We further investigated the effect of the PAS resonance wavelength (R_{plasmon}) on the enhancement of the DVP by performing PL measurements on WS₂-2TRHPAS heterostructures with three different resonance wavelengths $R_{\text{plasmon}} = 310$ nm (2.42×10^{14} Hz), 620 nm (4.84×10^{14} Hz), and 930 nm (7.26×10^{14} Hz), and the corresponding PL spectra and the DVP values are shown in Figure S10, Supporting Information. These results revealed the best RT DVP enhancement occurred at $R_{\text{plasmon}} = 620$ nm, which coincided with the neutral A-exciton emission wavelength.

Neutral excitons are the natural low-energy excitations of a charge-neutral semiconductor, whereas trions are only formed in the presence of excess charge. Therefore, the intensity of trion emissions is generally dependent on the amount of excess charge in the semiconductor. For this reason, trion emissions were usually not found in the PL spectra of our CVD-grown monolayer WS₂ samples unless a back gate voltage was applied. For the gated samples, the PL spectra typically exhibited additional emissions at 30–60 meV below the neutral excitonic line, which may be attributed to the emission from negatively charged trions (X⁻). Thus, by simply varying the applied back gate voltage, we were able to control the ratio between neutral exciton and charged trion emissions.

Figure 5a shows a schematic of a back-gated FET device based on WS₂-2TRHPAS and an SEM image of the top view of such a device. For a given gate voltage, there were two well-defined PL spectral components associated with the emission bands of the neutral excitons (X) and the negatively charged trions (X⁻). We found that the emission near 620 nm (2 eV) from neutral excitons (X) was dominant around the charge neutrality point at $V_{\text{Gate}} = 0$. The optimal line shape fitting for the spectral contributions was found to be a mixed Gaussian-Lorentzian function, as shown in Figure S11, Supporting Information, for WS₂ and Figure S12, Supporting Information, for WS₂-2TRHPAS, respectively. The PL spectral evolution of these two emission bands with the gate voltage is illustrated in Figures S13 and S14, Supporting Information, for as-grown 1L-WS₂, and in Figure 5b,c for WS₂-2TRHPAS. We note that the trion-to-exciton intensity ratios of both WS₂-2TRHPAS and 1L-WS₂ exhibited similar dependence on the gate voltage, as shown in Figure 5c and Figure S13c, Supporting Information, respectively.

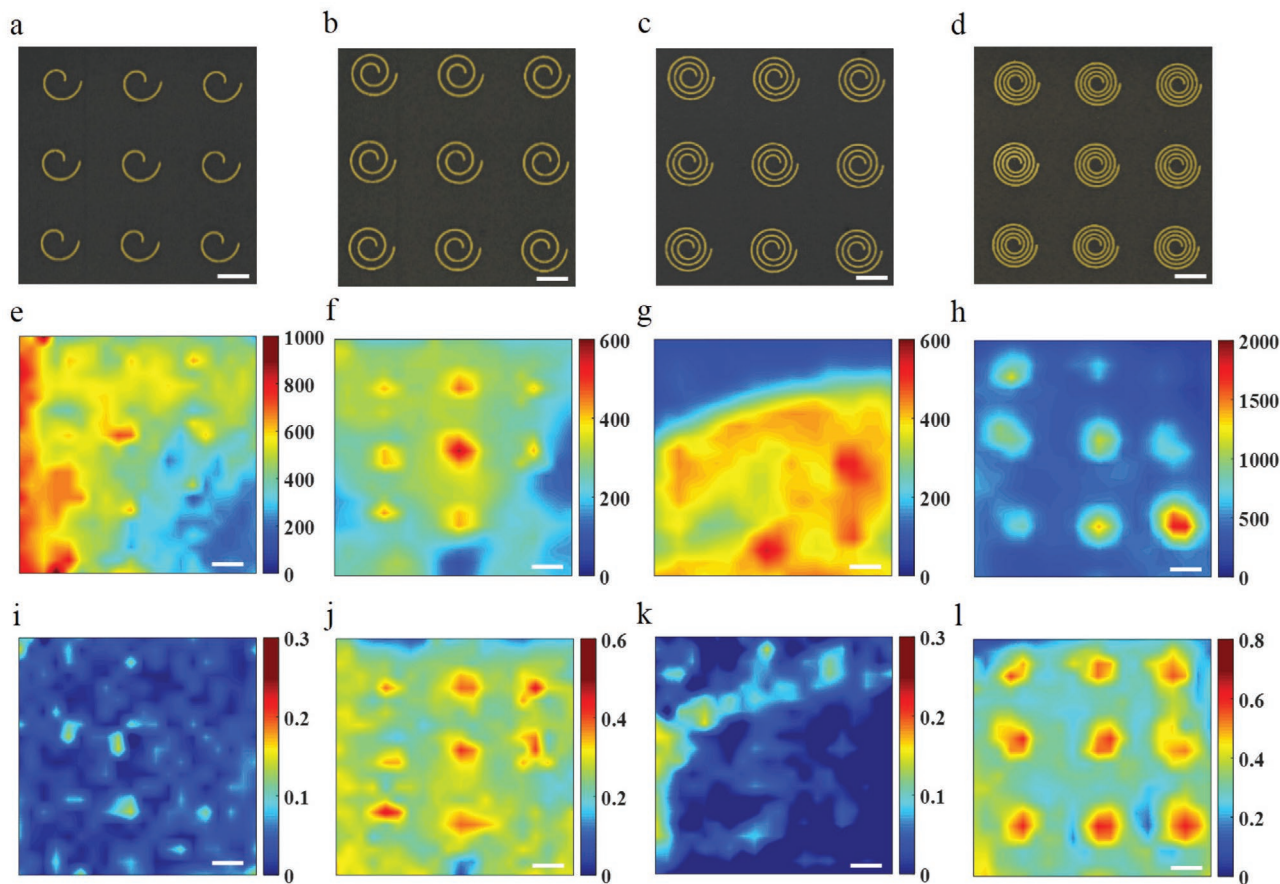


Figure 4. Dependence of the RT valley polarization of WS_2 -RHPAS structures on the ring number of PAS. a–d) SEM images of 1-, 2-, 3-, and 4-turn RHPAS arrays. (Scale bar: $1.25 \mu\text{m}$). e–h) PL intensity mapping of WS_2 samples with 1-, 2-, 3-, and 4-turn RHPAS arrays under σ^+ (RCP) excitation at 514 nm. Apparent focusing effects can be obtained from 2- and 4-turn RHPAS arrays, in contrast to the absence of focusing effects from 1- and 3-turn RHPAS arrays. (Scale bar: $1.25 \mu\text{m}$). i–l) Maps of the DVP taken on WS_2 with 1-, 2-, 3-, and 4-turn RHPAS arrays under the RCP excitation. Apparently high values of DVP can be obtained at RT from WS_2 with 2- and 4-turn RHPAS arrays (Scale bar: $1.25 \mu\text{m}$).

Figure S13a, Supporting Information, shows a color map of the PL spectra from a back-gated field-effect device of as-grown 1L- WS_2 with the back-gate voltages (V_{Gate}) from -25 to 25 V at RT. For negative gate voltages ($V_{\text{Gate}} < 0$), both X and X^- features were visible, and the integrated intensity of the X-peak gradually decreased while that of the X^- -peak increase when $|V_{\text{Gate}}|$ decreases. In contrast, for positive gate voltage ($V_{\text{Gate}} > 0$), the integrated intensity of the X-peak gradually decreased and the X^- -peak became dominant with increasing V_{Gate} due to electrostatic doping, which led to a single X^- -peak profile for sufficiently high carrier densities, implying that the Fermi level moved much closer to the energy of the bound trion states than to that of the neutral exciton states.

Helicity resolved PL spectra of an as-grown gated WS_2 sample are shown in Figures S14b and S14c, Supporting Information, for $V_{\text{Gate}} = -2$ V and $+5$ V, respectively. When the WS_2 sample was negatively gated at $V_{\text{Gate}} = -2$ V, both X and X^- emissions revealed relatively low DVP of 4.2% and 5.8%, respectively. Similarly, at a positive gate voltage ($V_{\text{Gate}} = 5$ V), both X and X^- emissions also revealed low DVP of 4.7% and 5.1%, respectively. These low DVP values implied that the significant intervalley scattering was insensitive to the gate voltage in the as-grown WS_2 sample.

In contrast to the small effect of the gate voltage on the DVP of the as-grown WS_2 sample, the gate voltage dependent DVP became significantly different in the case of 1L- WS_2 -2TRHPAS heterostructures. Figure 5b,c shows the PL spectral evolution of X and X^- emissions from the 1L- WS_2 -2TRHPAS sample with the gate voltage. Additionally, polarization-resolved PL spectra of the 1L- WS_2 -2TRHPAS sample under σ^+ excitations are shown in Figure 5d–f for $V_{\text{Gate}} = 0$, -10 V, and -20 V, respectively. For $V_{\text{Gate}} = 0$, the photon-excited excitons at the K valley were more populated under σ^+ excitations, which corresponded to the valley-polarized state in pristine WS_2 and WS_2 -2TRHPAS. By increasing the electron density via decreasing the gate voltage from 0 to -10 V and -20 V, the difference between the σ^+ and σ^- components of the PL spectra became more significant, implying increased valley polarization of the neutral excitons. Specifically, we found that the values of DVP for $V_{\text{Gate}} = 0$, -10 V, and -20 V were 40%, 50%, and 70%, respectively, suggesting significantly enhanced valley polarization as the applied bias was detuned from the charge neutral point. The corresponding RT spatially resolved DVP map and PL maps of a WS_2 -2TRHPAS device at $V_{\text{Gate}} = -20$ V are shown in Figure 5g and Figure S15, Supporting Information, respectively.

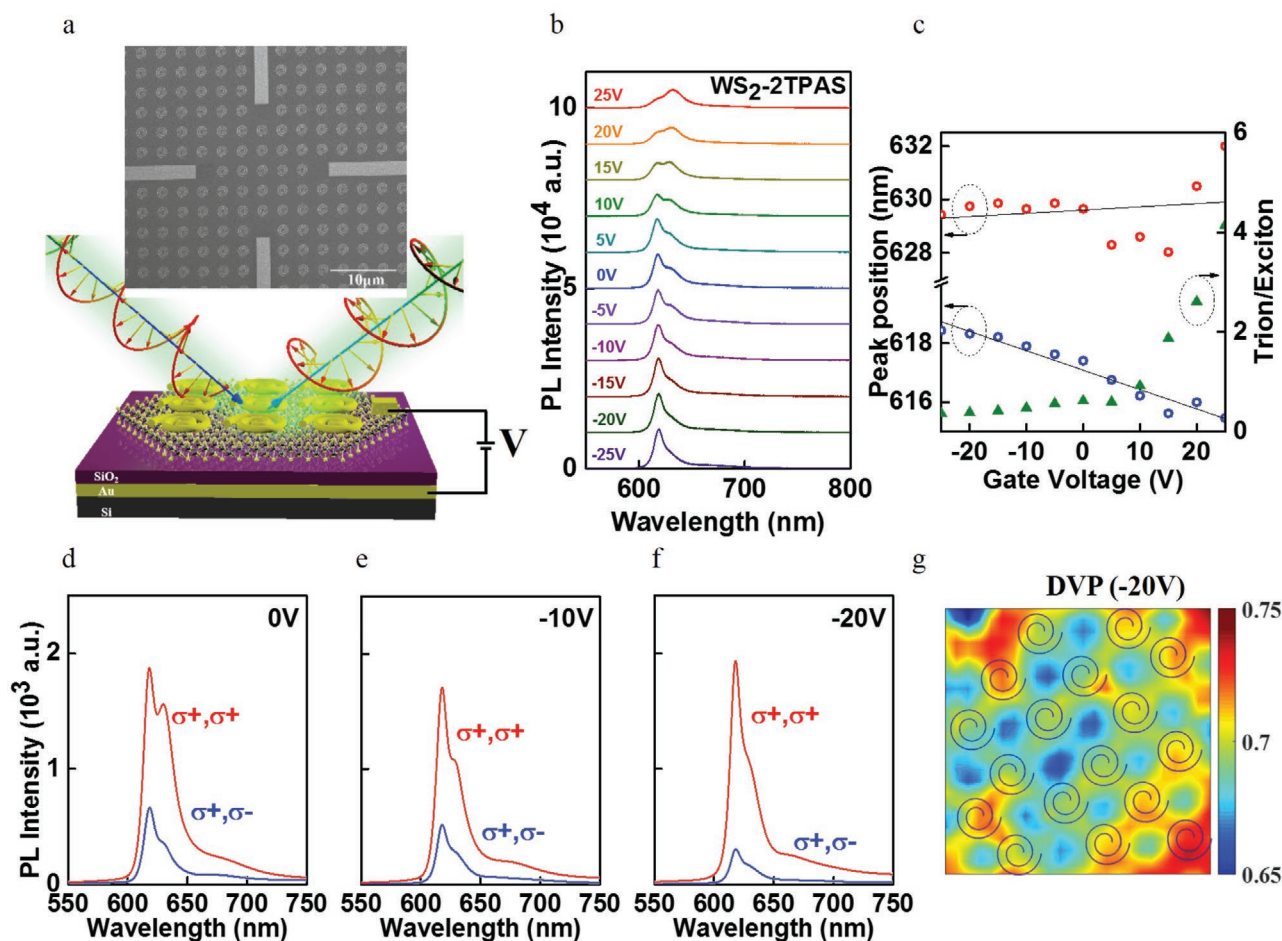


Figure 5. a) Electrically tunable valley polarization of WS₂-2TRHPAS heterostructure. b) PL spectra at RT for V_{Gate} from -25 V to 25 V, with an increment of 5 V. c) Gate voltage dependence of the PL peak position for neutral excitons (blue) and trions (red) under V_{Gate} from -25 V to 25 V. The intensity ratio of trions to excitons (green) is also shown as a function of V_{Gate} from -25 V to 25 V. d–f) The σ^+ (red) and σ^- (blue) PL intensity taken at RT under $V_{\text{Gate}} = 0$ (d), $V_{\text{Gate}} = -10$ V (e), and $V_{\text{Gate}} = -20$ V (f), respectively. g) Spatial map of the DVP in a WS₂-2TRHPAS heterostructure under $V_{\text{Gate}} = -20$ V at RT.

To gain further insights into this behavior, we performed gate-dependent transport measurements, using a scheme where a positive bias induced hole-doping and a negative bias introduced electron-doping. We observed typical n-type transport behavior with on/off current ratios greater than 10^4 at RT, as shown in Figure S16, Supporting Information. The doped carrier density n under gate voltage V_{Gate} was estimated from the geometric capacitance and back-gate voltage using the following relation

$$n = (\epsilon\epsilon_0 / t_{\text{ox}})(V_{\text{Gate}} - V_{\text{CNP}}) / e \quad (2)$$

where $\epsilon = 3.9$ is the dielectric constant of SiO₂, t_{ox} is the thickness of SiO₂, and ϵ_0 is the vacuum permittivity. As shown in Figure S16, Supporting Information, the charge neutral point (CNP) was observed to be at 2 V so that the n-type carrier concentration could be estimated by using Equation (2), which yielded $-7.19 \times 10^{11} \text{ cm}^{-2}$, $-4.31 \times 10^{12} \text{ cm}^{-2}$, and $-7.91 \times 10^{12} \text{ cm}^{-2}$ for 0 V, -10 V, and -20 V, respectively. Given a carrier concentration n , the corresponding Fermi-level position could be estimated by using the following expression for semiconductors:

$$E_f - E_c = k_B T \ln(e^{n/g_{2D}k_B T} - 1) \quad (3)$$

where E_f is the Fermi-level energy, E_c is the conduction band edge, $g_{2D} = g_v m^* / \pi \hbar^2$ is the density of states, g_v is the valley degeneracy factor, and $m^* = 0.34m_0$. Therefore, the Fermi-level position was estimated to be 0.3 eV, 0.25 eV, and 0.23 eV lower than the conduction band minimum for 0 V, -10 V, and -20 V, respectively. As shown in Figure 5d–f, the degree of valley polarization steadily increased with the carrier density at RT, which may be attributed to the noticeable screening effect by the doped carriers.

Specifically, the mechanism for the enhancement of valley polarization by electrostatic doping in the WS₂-2TRHPAS heterostructure may be attributed to carrier doping-induced suppression on the intervalley relaxation process. The intervalley relaxation process of bright excitons is dominated by the long range electron–hole (e–h) exchange interaction, and the long-range e–h exchange interactions can be efficiently screened by adding 2D electrons/holes with electrostatic doping.^[55] The screen length is determined by the inverse of the Thomas–Fermi wave vector, which is given by the following expression:^[55]

$$k_{\text{TF}}(T, E_f) = k_{\text{TF0}} \left[1 - e^{-(E_f/k_B T)} \right] \quad (4)$$

where $k_{\text{TF0}} = \sqrt{g_s g_v m^* e^2 / (4\pi\epsilon\hbar^2)}$ is the zero temperature Thomas–Fermi wave vector, g_s (g_v) are the degeneracy for spins (valleys), m^* is the effective electron or hole mass, and ϵ is the dielectric constant. The Fermi energy E_f measured from the bottom of the conduction band (to the top of the valence band) is defined by $E_f = 2\pi n \hbar^2 / (g_s g_v m^*)$, where n is the doped electron (hole) density. Therefore, k_{TF} increases rapidly with increasing n according to Equation (4). In the strong scattering limit, the intervalley scattering rate $(\tau_v)^{-1}$ due to e–h exchange interaction may be approximated by the relation $(\tau_v)^{-1} \propto (k_{\text{TF}})^{-2}$.^[55] Therefore, the intervalley scattering rate $(\tau_v)^{-1}$ is strongly suppressed by carrier doping. In contrast, the intra-valley relaxation time τ_0 is much less affected by carrier doping, as supported by the stable linewidths and integrated intensities upon doping.^[56] Our work aims to tailor the degree of valley polarization by manipulating the intervalley scattering rate $(\tau_v)^{-1}$ via tuning the carrier doping. Noting that the valley polarization P_{DVP} ^[57] is given by

$$P_{\text{DVP}} = \frac{P_0}{1 + 2(\tau_0 / \tau_v)} \quad (5)$$

where P_0 is the ideal valley polarization, we find that the suppression of $(\tau_v)^{-1}$ by electrostatic doping leads to the enhancement of P_{DVP} , which agrees well with our experimental observations.

3. Conclusion

We have demonstrated that ultracompact PAS nanostructures can efficiently tailor the valley-polarized PL of monolayer WS_2 at RT. The chiral-SPP focusing fields from the PAS nanostructures can significantly amplify the exciton/trion emissions in the WS_2 monolayer with specific chiral emission due to the interaction of WS_2 excitons/trions with the plasmons of the PAS nanostructures. The plasmon–exciton coupling is shown to provide control of the valley-polarized PL through manipulating the imbalance of valley population, leading to significant PL modulations through valley-dependent control of the excitonic emissions at RT. In particular, we have demonstrated enhancement of the DVP at RT from $\approx 3\%$ for the as-grown 1L- WS_2 to $\approx 40\%$ for the 1L- WS_2 –2TRHPAS heterostructures and to $\approx 50\%$ for the 1L- WS_2 –4TRHPAS heterostructures. Furthermore, by applying a back-gate bias voltage (V_{Gate}), the valley polarization is found to be further enhanced from 40% to 70% for $V_{\text{Gate}} = -20$ V, which implies that the excess carrier doping can enhance the valley polarization by screening of the momentum-dependent long-range electron–hole exchange interaction and therefore reducing the intervalley scattering. The methodology described in this work provides a promising platform to manipulate the valley degrees of freedom in 2H-TMDs efficiently at RT, paving ways for future applications of opto-valleytronic/spintronic devices based on these 2D materials.

4. Experimental Section

Synthesis of WS_2 : Monolayer WS_2 was grown by using APCVD as reported previously. 95 mg WO_3 precursor mixed with 5 mg KI was

placed in a quartz boat containing the SiO_2/Si substrates that were set face-down directly above the W source precursor, and the quartz boat was then positioned at the center of the furnace. A second boat containing 100 mg S was placed upstream at 18 cm away from the W source. Next, the system was pump down to 3×10^{-2} Torr to eliminate air and moisture. After the system reached the base pressure, the Ar/H_2 (80/40 sccm) carrier gas was introduced until atmospheric pressure was achieved. The furnace was then heated up with a ramp rate of $35 \text{ }^\circ\text{C min}^{-1}$ to the growth temperatures (750 to 850 $^\circ\text{C}$). The S component melted at 150 $^\circ\text{C}$ was sent into the furnace at the growth temperature to grow WS_2 . The sample growth procedure proceeded for 10 min, after which the furnace was directly opened to RT to stop the reaction immediately.

Transfer of Mono- and Multilayer WS_2 : Polystyrene (PS) was used as the supplementary film to peel off the WS_2 crystals from sapphire substrates. PS (M.W. 192 000) dispersed in toluene solution (20 mg mL^{-1}) was spin-coated on top of the WS_2 sample at a speed of 3000 rpm. The edge of the PS film was scribed with a blade, and then the sample of PS/ WS_2 /Si-substrate was inserted into water slowly. The PS/ WS_2 film became peeled off naturally in water, and was subsequently rinsed with deionized-water thrice before it was picked up and placed onto the target substrate. The PS coating was removed with toluene after baking the sample at 80 $^\circ\text{C}$ for 60 min.

PL and TRPL Characterizations: The PL spectra were taken with a Renishaw InVia Raman spectrometer system using a 514.3 nm laser (2.41 eV) as the excitation source. A 50 \times objective lens with a numerical aperture of 0.75 and a 2400 and 1800 lines/mm grating were chosen during the measurement to achieve better signal-to-noise ratio. The time-resolved PL measurements were taken on an inverted microscope (Zeiss Axio Observer) equipped with an avalanche photodiode (Picoquant PDM series with PicoHarp 300 timing electronics). For the PL lifetime measurements, a 532 nm picosecond laser diode (70 ps pulse duration, 40 MHz repetition rate; PicoQuant) excitation source was used, and a 532 nm band pass filter was placed after laser source to purify the laser beam. A 100 \times objective lens with a numerical aperture of 0.9 (Zeiss, Inc.) was used to focus the pulsed laser to a small spot of $1.6 \times 10^{-6} \text{ cm}^2$ with an estimated peak power density of 7.5 kW cm^{-2} .

Device Preparation and Device Measurements: The MDMs were fabricated on a heavily p-doped Si substrate via an E-beam evaporator and PECVD. The 150 nm-thick gold mirror layer was deposited on the heavily p-doped Si substrate by E-beam evaporation. Then, a thin silicon oxide (≈ 10 nm) layer was deposited by PECVD. After forming 10 nm SiO_2 layer on top of the Au/Si substrate, an annealing treatment in Ar at 1050 $^\circ\text{C}$ for 5 h was followed by the growth of an additional oxide to the final thickness (60 nm). The CVD-grown WS_2 was transferred on to the dielectric spacer using the method described above. Lastly, the Archimedes spiral rings were patterned by E-beam lithography on a 50 nm-thick Au film deposited on the WS_2 –PAS. The electrical properties of the WS_2 –2TRHPAS FETs were studied using a Keithley 2636 sourcemeter as a DC voltage source in vacuum at 300 K.

Supporting Information

Supporting Information is available from the Wiley Online Library or from the author.

Acknowledgements

This work was jointly supported by the Army Research Office under the Multi-University Research Initiative (MURI) program (award #W911NF-16-1-0472) and the National Science Foundation under the Physics Frontier Center program for Institute for Quantum Information and Matter (IQIM) at the California Institute of Technology (award #1733907). The authors are also grateful for the support from the Beckman Institute at the California Institute of Technology for access to facilities at the Molecular Materials Research Center. W.-H.L. acknowledges a graduate

fellowship from the J. Yang Family Foundation. P.C.W. acknowledges the support from the Ministry of Science and Technology (MOST), Taiwan (Grant number: 107-2923-M-006-004-MY3; 108-2112-M-006-021-MY3; 110-2124-M-006-004), and in part from the Higher Education Sprout Project of the Ministry of Education (MOE) to the Headquarters of University Advancement at National Cheng Kung University (NCKU). P.C.W. also acknowledges the support from the Ministry of Education (Yushan Young Scholar Program). The authors also thank Wen-Hui Cheng for training on the atomic layer deposition (ALD) system.

Conflict of Interest

The authors declare no conflict of interest.

Data Availability Statement

Research data are not shared.

Keywords

chiral plasmonic metasurface, circular dichroism, exciton–plasmon interaction, transition metal dichalcogenides, valleytronics

Received: June 25, 2021

Revised: October 3, 2021

Published online:

- [1] K. F. Mak, C. Lee, J. Hone, J. Shan, T. F. Heinz, *Phys. Rev. Lett.* **2010**, *105*, 136805.
- [2] A. Splendiani, L. Sun, Y. Zhang, T. Li, J. Kim, C.-Y. Chim, G. Galli, F. Wang, *Nano Lett.* **2010**, *10*, 1271.
- [3] S. Z. Butler, S. M. Hollen, L. Cao, Y. Cui, J. A. Gupta, H. R. Gutiérrez, T. F. Heinz, S. S. Hong, J. Huang, A. F. Ismach, E. Johnston-Halperin, M. Kuno, V. V. Plashnitsa, R. D. Robinson, R. S. Ruoff, S. Salahuddin, J. Shan, L. Shi, M. G. Spencer, M. Terrones, W. Windl, J. E. Goldberger, *ACS Nano* **2013**, *7*, 2898.
- [4] R. Ganatra, Q. Zhang, *ACS Nano* **2014**, *8*, 4074.
- [5] J.-K. Huang, J. Pu, C.-L. Hsu, M.-H. Chiu, Z.-Y. Juang, Y.-H. Chang, W.-H. Chang, Y. Iwasa, T. Takenobu, L.-J. Li, *ACS Nano* **2014**, *8*, 923.
- [6] Q. H. Wang, K. Kalantar-Zadeh, A. Kis, J. N. Coleman, M. S. Strano, *Nat. Nanotechnol.* **2012**, *7*, 699.
- [7] F. Xia, H. Wang, D. Xiao, M. Dubey, A. Ramasubramaniam, *Nat. Photonics* **2014**, *8*, 899.
- [8] H. Zeng, J. Dai, W. Yao, D. Xiao, X. Cui, *Nat. Nanotechnol.* **2012**, *7*, 490.
- [9] K. F. Mak, K. He, J. Shan, T. F. Heinz, *Nat. Nanotechnol.* **2012**, *7*, 494.
- [10] T. Cao, G. Wang, W. Han, H. Ye, C. Zhu, J. Shi, Q. Niu, P. Tan, E. Wang, B. Liu, J. Feng, *Nat. Commun.* **2012**, *3*, 887.
- [11] D. Xiao, G.-B. Liu, W. Feng, X. Xu, W. Yao, *Phys. Rev. Lett.* **2012**, *108*, 196802.
- [12] G. Wang, A. Chernikov, M. M. Glazov, T. F. Heinz, X. Marie, T. Amand, B. Urbaszek, *Rev. Mod. Phys.* **2018**, *90*, 021001.
- [13] W.-H. Lin, W.-S. Tseng, C. M. Went, M. L. Teague, G. R. Rossman, H. A. Atwater, N.-C. Yeh, *ACS Nano* **2020**, *14*, 1350.
- [14] D. Xiao, W. Yao, Q. Niu, *Phys. Rev. Lett.* **2007**, *99*, 236809.
- [15] W. Yao, D. Xiao, Q. Niu, *Phys. Rev. B* **2008**, *77*, 235406.
- [16] J. S. Ross, S. Wu, H. Yu, N. J. Ghimire, A. M. Jones, G. Aivazian, J. Yan, D. G. Mandrus, D. Xiao, W. Yao, X. Xu, *Nat. Commun.* **2013**, *4*, 1474.
- [17] M. Schadt, *Annu. Rev. Mater. Sci.* **1997**, *27*, 305.
- [18] L. Albani, C. Marchessoux, T. Kimpe, *Inf. Disp.* **2011**, *27*, 24.
- [19] R. Farshchi, M. Ramsteiner, J. Herfort, A. Tahraoui, H. T. Grahn, *Appl. Phys. Lett.* **2011**, *98*, 162508.
- [20] K. Hammerer, A. S. Sørensen, E. S. Polzik, *Rev. Mod. Phys.* **2010**, *82*, 1041.
- [21] R. Ursin, T. Jennewein, M. Aspelmeyer, R. Kaltenbaek, M. Lindenthal, P. Walther, A. Zeilinger, *Nature* **2004**, *430*, 849.
- [22] G. Wang, E. Palleau, T. Amand, S. Tongay, X. Marie, B. Urbaszek, *Appl. Phys. Lett.* **2015**, *106*, 112101.
- [23] W. Yang, J. Shang, J. Wang, X. Shen, B. Cao, N. Peimyo, C. Zou, Y. Chen, Y. Wang, C. Cong, W. Huang, T. Yu, *Nano Lett.* **2016**, *16*, 1560.
- [24] A. M. Jones, H. Yu, N. J. Ghimire, S. Wu, G. Aivazian, J. S. Ross, B. Zhao, J. Yan, D. G. Mandrus, D. Xiao, W. Yao, X. Xu, *Nat. Nanotechnol.* **2013**, *8*, 634.
- [25] Z. Wang, Z. Dong, Y. Gu, Y.-H. Chang, L. Zhang, L.-J. Li, W. Zhao, G. Eda, W. Zhang, G. Grinblat, S. A. Maier, J. K. W. Yang, C.-W. Qiu, A. T. S. Wee, *Nat. Commun.* **2016**, *7*, 11283.
- [26] Y. You, X.-X. Zhang, T. C. Berkelbach, M. S. Hybertsen, D. R. Reichman, T. F. Heinz, *Nat. Phys.* **2015**, *11*, 477.
- [27] W.-T. Hsu, Y.-L. Chen, C.-H. Chen, P.-S. Liu, T.-H. Hou, L.-J. Li, W.-H. Chang, *Nat. Commun.* **2015**, *6*, 8963.
- [28] S. Wu, J. S. Ross, G.-B. Liu, G. Aivazian, A. Jones, Z. Fei, W. Zhu, D. Xiao, W. Yao, D. Cobden, X. Xu, *Nat. Phys.* **2013**, *9*, 149.
- [29] G. Aivazian, Z. Gong, A. M. Jones, R.-L. Chu, J. Yan, D. G. Mandrus, C. Zhang, D. Cobden, W. Yao, X. Xu, *Nat. Phys.* **2015**, *11*, 148.
- [30] Y. Li, J. Ludwig, T. Low, A. Chernikov, X. Cui, G. Arefe, Y. D. Kim, A. M. van der Zande, A. Rigosi, H. M. Hill, S. H. Kim, J. Hone, Z. Li, D. Smirnov, T. F. Heinz, *Phys. Rev. Lett.* **2014**, *113*, 266804.
- [31] D. MacNeill, C. Heikes, K. F. Mak, Z. Anderson, A. Kormányos, V. Zólyomi, J. Park, D. C. Ralph, *Phys. Rev. Lett.* **2015**, *114*, 037401.
- [32] K. F. Mak, J. Shan, *Nat. Photonics* **2016**, *10*, 216.
- [33] A. Srivastava, M. Sidler, A. V. Allain, D. S. Lembke, A. Kis, A. Imamoglu, *Nat. Phys.* **2015**, *11*, 141.
- [34] H.-T. Lin, C.-Y. Chang, P.-J. Cheng, M.-Y. Li, C.-C. Cheng, S.-W. Chang, L. L. J. Li, C.-W. Chu, P.-K. Wei, M.-H. Shih, *ACS Appl. Mater. Interfaces* **2018**, *10*, 15996.
- [35] T. Wen, W. Zhang, S. Liu, A. Hu, J. Zhao, Y. Ye, Y. Chen, C.-W. Qiu, Q. Gong, G. Lu, *Sci. Adv.* **2020**, *6*, ea00019.
- [36] Q. Jiang, B. Du, M. Jiang, D. Liu, Z. Liu, B. Li, Z. Liu, F. Lin, X. Zhu, Z. Fang, *Nanoscale* **2020**, *12*, 5906.
- [37] J. Sun, H. Hu, D. Pan, S. Zhang, H. Xu, *Nano Lett.* **2020**, *20*, 4953.
- [38] K. Shinokita, X. Wang, Y. Miyauchi, K. Watanabe, T. Taniguchi, K. Matsuda, *Adv. Funct. Mater.* **2019**, *29*, 1900260.
- [39] Z. Li, Y. Li, T. Han, X. Wang, Y. Yu, B. Tay, Z. Liu, Z. Fang, *ACS Nano* **2017**, *11*, 1165.
- [40] Z. Li, C. Liu, X. Rong, Y. Luo, H. Cheng, L. Zheng, F. Lin, B. Shen, Y. Gong, S. Zhang, Z. Fang, *Adv. Mater.* **2018**, *30*, 1801908.
- [41] Z. Wu, J. Li, X. Zhang, J. M. Redwing, Y. Zheng, *Adv. Mater.* **2019**, *31*, 1904132.
- [42] M. Deng, X. Wang, J. Chen, Z. Li, M. Xue, Z. Zhou, F. Lin, X. Zhu, Z. Fang, *Adv. Funct. Mater.* **2021**, *31*, 2010234.
- [43] L. Zheng, Z. Liu, D. Liu, X. Wang, Y. Li, M. Jiang, F. Lin, H. Zhang, B. Shen, X. Zhu, Y. Gong, Z. Fang, *Nat. Commun.* **2021**, *12*, 291.
- [44] V. K. Valev, N. Smisdom, A. V. Silhanek, B. De Clercq, W. Gillijns, M. Ameloot, V. V. Moshchalkov, T. Verbiest, *Nano Lett.* **2009**, *9*, 3945.
- [45] M. Kuwata-Gonokami, N. Saito, Y. Ino, M. Kauranen, K. Jefimovs, T. Vallius, J. Turunen, Y. Svirko, *Phys. Rev. Lett.* **2005**, *95*, 227401.
- [46] M. J. Huttunen, G. Bautista, M. Decker, S. Linden, M. Wegener, M. Kauranen, *Opt. Mater. Express* **2011**, *1*, 46.
- [47] M. Decker, R. Zhao, C. M. Soukoulis, S. Linden, M. Wegener, *Opt. Lett.* **2010**, *35*, 1593.
- [48] E. Plum, X.-X. Liu, V. A. Fedotov, Y. Chen, D. P. Tsai, N. I. Zheludev, *Phys. Rev. Lett.* **2009**, *102*, 113902.

- [49] C. Zhang, K. Wu, V. Giannini, X. Li, *ACS Nano* **2017**, *11*, 1719.
- [50] A. Belardini, M. C. Larciprete, M. Centini, E. Fazio, C. Sibilìa, D. Chiappe, C. Martella, A. Toma, M. Giordano, F. Buatier de Mongeot, *Phys. Rev. Lett.* **2011**, *107*, 257401.
- [51] N. Meinzer, E. Hendry, W. L. Barnes, *Phys. Rev. B* **2013**, *88*, 041407.
- [52] M. Cotrufo, C. I. Osorio, A. F. Koenderink, *ACS Nano* **2016**, *10*, 3389.
- [53] V. K. Valev, J. J. Baumberg, C. Sibilìa, T. Verbiest, *Adv. Mater.* **2013**, *25*, 2517.
- [54] S. Kühn, U. Håkanson, L. Rogobete, V. Sandoghdar, *Phys. Rev. Lett.* **2006**, *97*, 017402.
- [55] S. Konabe, *Appl. Phys. Lett.* **2016**, *109*, 073104.
- [56] S. Mouri, Y. Miyauchi, K. Matsuda, *Nano Lett.* **2013**, *13*, 5944.
- [57] S. Feng, C. X. Cong, S. Konabe, J. Zhang, J. Z. Shang, Y. Chen, C. J. Zou, B. C. Cao, L. S. Wu, N. Peimyoo, B. L. Zhang, T. Yu, *Small* **2019**, *15*, 1805503.